Proceedings of the 8th International Conference on MicroManufacturing
University of Victoria, Victoria, BC, Canada, March 25-28, 2013

Stochastic Characteristics in Microgrinding Wheel Static Topography using Machine Vision

ICOMM
2013
No. 120

Jacob Kunz[1], and J. Rhett Mayor[2]
[1]Jacob Kunz; George W. Woodruff School of Mechanical Engineering, Georgia Institute of Technology, USA; jacobakunz@gatech.edu
[2]J. Rhett Mayor; George W. Woodruff School of Mechanical Engineering, Georgia Institute of Technology, USA; j.rhett.mayor@me.gatech.com

Key Words: Grinding, Microgrinding, Stochastic Modeling

ABSTRACT

Superabrasive grinding wheels are used for the machining of brittle materials such tungsten carbide. Stochastic modeling of the wheel topography can allow for statistical bounding of the grind force characteristics allowing improved surface quality without sacrificing productivity. This study utilizes a machine vision method to measure the wheel topography of diamond microgrinding wheels. The results showed that there are large variances in wheel specifications from the manufacturer. The numerical simulation and analytic models used to describe the wheel topography were seen to estimate the static grit density to within 4.5% using measured wheel geometry specifications. Utilizing only manufacturer-supplied specifications caused the models to predict the static grit density to within 24% leading to a need for improved wheel tolerancing and *in situ* wheel measurement.

INTRODUCTION

Superabrasive grinding wheels are used for the machining of hard materials using various grinding approaches. The brittle nature of workpieces such as tungsten carbide require ductile-regime material removal through grinding with grits that have a large diameter to depth-of-cut ratio [2]. The fracture sensitivity of brittle workpieces to chip load and the desire for improved final geometric accuracy leads to the need for improved process modeling and understanding.

Grinding wheels consist of cutting edges whose size, shape, location, and dynamic interaction are stochastically random [3-5]. Metrics describing the wheel topography consist of the static grit density, which describes the number of grits per unit area on the wheel surface, and the dynamic grit density which describes the number of actively cutting grits per unit wheel surface area during the cutting process. The cutting rake angle and undeformed chip thickness further specify the characteristics of the material removal mechanics during the cutting of each individual grit.

Conventional superabrasive grinding wheels contain grits that number on the order of hundreds of thousands. Such large grit populations in single wheels lend their topographical characterization to be sufficiently described by single-value metrics. Microgrinding wheels, or grinding pins, are defined as superabrasive wheels that have diameters less than ¼" but still utilize conventional grit sizes as seen on the surface of a #220, 1mm OD wheel in Fig. 1. This leads to a small number of grits residing in the wheel creating a need to expand topography descriptions to include stochastic information beyond single-value averages.

The impact of manufacturing variances in wheel characteristics are also of keen interest as they directly affect the process variation between wheels. Conventional grinding wheels utilize truing procedures to conform the wheel diameter to tolerance but single-layered electroplated wheels are not trued but rely on the manufacturer accuracy. In addition, the ability to control the grit concentration in electroplated wheels is not well documented so the impact of manufacturing variations of concentration number is not known. Micro-scale grinding wheels can be especially susceptible to these variations due to the few number of grits within each wheel.

This paper will investigate the effect of scaling down the diameter of grinding wheels with respect to the grits. An ANOVA study is conducted on a set of microgrinding wheels from a single manufacturer to characterize the nature of manufacturing variances. Machine vision techniques are used to inspect surface grits on the microgrinding wheels. Full imaging of wheel surfaces is used to calculate the number of grits in each wheel, the linear spacing between the grits, and the wheel static grit density. Finally, the relationship between manufacturing variance and static wheel topography variance is examined.

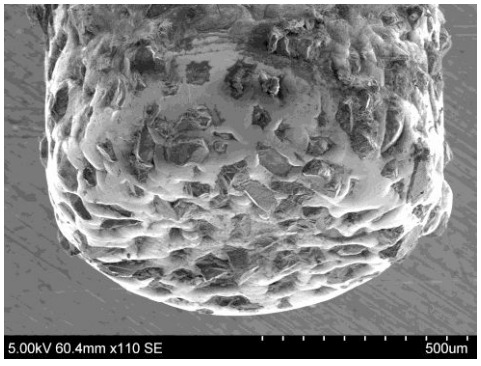

Fig. 1: SEM Image of 1mm OD, Metal Bonded, #220 Grit Diamond Grinding Wheel.

MACHINE VISION INSPECTION AND MEASUREMENT OF MICROGRINDING WHEELS

A. BACKGROUND OF STOCHASTIC TOPOGRAPHY MODELING

Many studies have generated models for the static topography of grind wheel surfaces. Fundamental stochastic modeling has used uniformly distributed grits on the wheel surface to calculate a negative exponential distribution of the static inter-grit spacings on the wheel surface [6-9]. Static wheel measurements by Hwang and Evans showed that the distribution of the grit protrusion height above the bond surface in electroplated diamond wheels can be modeled using a Gaussian distribution [10].

Prior work by the authors showed a new model for the static grit density in the wheel that utilizes base assumptions about the distribution of grit size and location. The model provided a fully analytic calculation of the static grit density calculation. In addition, a more advanced numerical simulation model was generated to capture more accurately the nature of the grit locations within the wheel [11]. A goal of this current study is to investigate experimentally the accuracy of the analytic and numerical simulation models.

B. IMAGING OF WHEEL SURFACE

The grinding wheels measured are single-layered, electroplated wheels with medium diamond grits. Images of the grinding wheels were taken under a standard microscope. An example raw image of a wheel is shown in Fig. 2 under 10x magnification. Each image only provides a view of a 75 µm-wide strip of in-focus grits in the center of the image. A full image of the wheel was obtained by taken sequential images as the wheel was rotated under the microscope. The images were digitally stitched together by manually matching control points on grits that appear in multiple images. A resulting full surface image is shown in Fig. 3 comprised of 61 stitched images. Wheels with large axial widths required multiple rows of images to be stitched together.

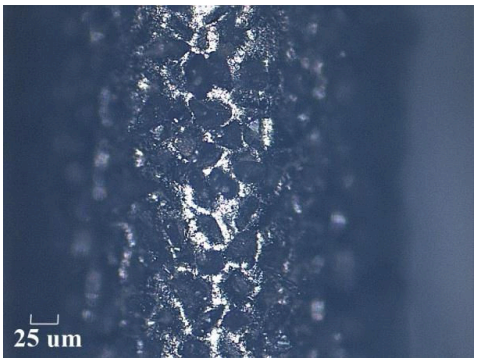

Fig. 2: Microscope Image of 1mm OD, #220 Grit Diamond Grinding Wheel in a Microscope at 10x Magnification.

Fig. 3: Stitched Imaged Surface of 0.5mm OD, #120 Grit Diamond Grinding Wheel.

C. MACHINE VISION ANALYSIS OF FULLY IMAGED WHEELS

The stitched images were analyzed using an automated machine vision algorithm previously developed and investigated by the authors [12]. The algorithm is summarized in Fig. 4 where the converted binary image is modified using erosion to remove small dark spots in the background wheel bond. An example of the effects of the analysis algorithm is shown in Fig. 5 for the #220 grit wheel where the grits are correctly identified along with their centroids.

The investigation inspected wheels of differing diameters, axial widths, and grit sizes as shown in experimental plan in Table 1. The manufacturer provided the target specifications for the wheel geometry along with the expected concentration number *C* achieved by the electroplating process. The expected numbers of abrasives in the wheels were calculated using an analytic stochastic model, shown in Eq. 1, that was generated by the authors in prior studies based on the standard definition of the wheel concentration. In addition, the expected static grit density on the wheel surface was predicted using analytic stochastic methods [11].

$$\mathrm{E}[N_\mathrm{a}] = \frac{3\mathrm{C}w\left(\frac{d_\mathrm{w}^2 - d_\mathrm{c}^2}{4}\right)}{200\mu_\mathrm{D}(\mu_\mathrm{D}{}^2 + 3\sigma_\mathrm{D}{}^2)} \qquad (1)$$

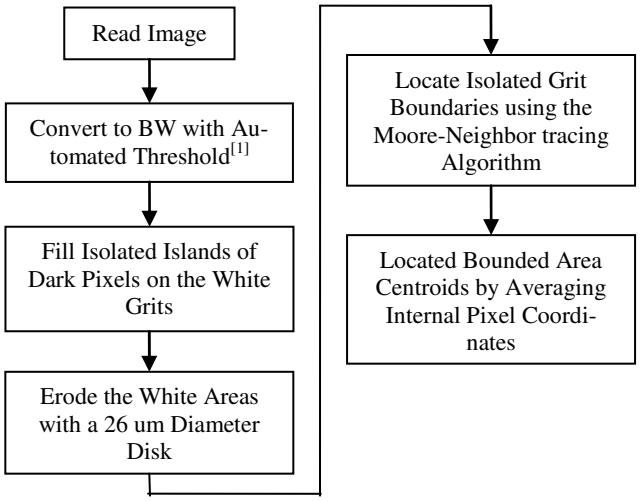

Fig. 4: Machine Vision Algorithm for Locating Individual Grits

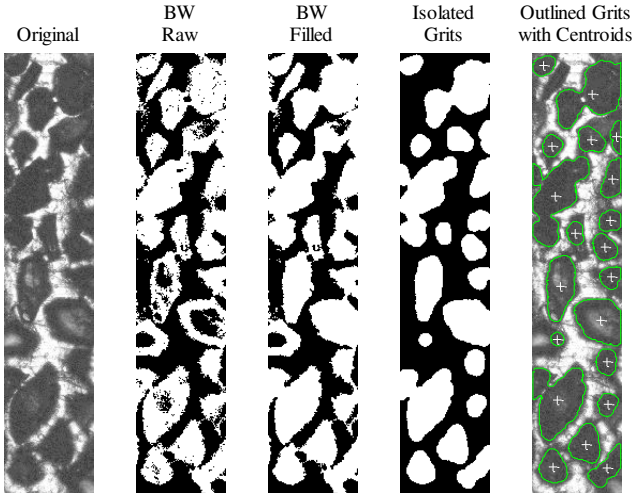

Fig. 5: Machine Vision Process for Analyzing Static Grit Locations

RESULTS

A. WHEEL SPECIFICATION ACCURACY

The grind wheels were optically measured on the microscope for accuracy in specified diameter and length while the unknown specification of the bond thickness was measured. The repeatability of the optical measurement method was measured to be ±0.9 µm by repeated measurement of a gauge pin. The complete results of the measured wheel specifications are shown in Table 3 in the appendix.

The ANOVA analysis of the measured microgrinding wheel specifications examined the relationships between the specifications set by the manufacturer, or the input factors, and the measured specification errors, or responses. An example of a single relationship analysis is the impact of the nominal wheel diameter on the bond thickness as shown in Fig. 6.

Table 1: Experimental Plan of Inspected Wheels

Wheel Set #	# of replicates	G#	OD [µm]	w [µm]	C
1	3	#200	508	1588	140
2	3	#400	508	3175	140
3	15	#400	1016	1588	140
4	6	#400*	1016	1588	140
5	3	#400	1016	3175	140
6	3	#400*	1016	3175	140
7	3	#400	1524	1588	140
8	3	#200	1524	3175	140

The 95% confidence intervals of the estimated mean bond thickness for each group are seen to overlap one another indicating that no conclusion can be made that the mean bond thickness is different for wheels of different diameters. A Tukey-Kramer test showed that the actual probability of the means being different (a Type I error has occurred) is 1.9%. The chosen family error rate limit for this study is chosen to be 5% so it is concluded that the bond thickness does not differ between wheels of different diameters.

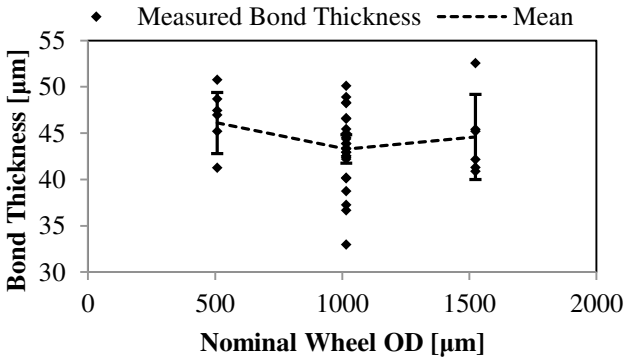

Fig. 6: Bond Thickness Measurements Showed no Definite Variation across Different Wheel Diameters with 95% Confidence

The concentration number for each wheel had to be calculated using the measured shank diameter, wheel width, and bond thickness. It had to be assumed that all of the grits embedded into the wheel bond protruded the outer surface allowing them to be counted using the machine vision measurement method. The concentration number was then calculated using Eq. 1 while the uncertainty in the calculated concentration numbers was determined by using Kline-Mclintock error propagation with the dimensional errors set as the ±0.9 µm repeatability of the measurement system. The uncertainty in the concentration numbers was calculated to be an average of 1.08 across all measured wheels.

The ANOVA analysis was executed on all factor combina-

tions in the experimental set to determine the impact of each factor on the wheel specification responses. The results are summarized in Table 2 where the response directions of the measured wheel specifications for increasing input factors are shown. Only four out of twelve interactions were seen to have significant impact according to the Tukey-Kramer test criteria.

Table 2: Experimental Plan of Inspected Wheels

			Manufacturer Specification				
			Grit #	OD	Width	μ	σ
			$\widehat{G}\uparrow$	$\widehat{D}\uparrow$	$\widehat{w}\uparrow$		
Measured Specification	Shank OD error	ε_{shank} [μm]	-	-	-	-5.2	10.1
	Axial Width error	ε_{width} [μm]	-	↓	↓	-189.6	160.6
	Bond Thickness	t [μm]	-	-	-	43.8	3.7
	Concentration # error	ε_C	-	↓	↑	-7.7	17.1

The mean and standard deviation were also calculated for each wheel specification across the entire set of wheels. An Anderson-Darling statistical test for each measured specification showed that they could each be described by a Gaussian distribution despite the four significant factor interactions. An example of one of the tests in shown in Fig. 7 with the all of the measured concentration numbers falling within the envelope of error of the population mean and standard deviation. The Anderson-Darling statistic for this particular test was 0.28 while the probability value (p-value) for the test was 63%, well above the chosen 5% threshold indicating that the Gaussian distribution cannot be rejected as the underlying distribution of this population. Tests of the other measured wheel specifications returned similar results allowing for each of them to be modeled with Gaussian distributions independent of the input factors.

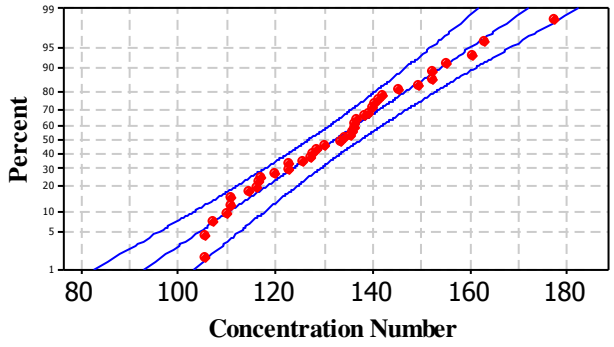

Fig. 7: Normal Probability Plot for the Measured Wheel Concentration Number across all Wheels

B. STATIC GRIT DENSITY MODEL ACCURACY

The static grit density was calculated for each measured wheel using the number of abrasives identified by the machine vision algorithm along with the measured wheel geometry specifications as shown in Eq. 2. The measured number of grits and static grit density for each wheel are included in Table 3 in the appendix.

$$C_s = \frac{N_a}{w\pi(D_{shank} + 2t)} \tag{2}$$

The accuracy of the analytic and numerical simulation models previously developed by the authors was measured by calculating the relative error between the measured values and model values. This is shown in Eq. 3 where μ_{C_s} is the modeled value and y_{C_s} is the measured value.

$$\varepsilon_{C_s} = \left(\frac{\mu_{C_s} - y_{C_s}}{y_{C_s}}\right) \times 100\% \tag{3}$$

The analytic and numerical simulation models show that for identical wheel geometries with identical concentration numbers, the static grit density for the separate wheels has a Gaussian distribution. The distribution of static grit densities is caused by the stochastic nature of the grit sizes and locations. The modeled value used in Eq. 3 is the mean of the modeled static grit density distribution. The distribution of the numerical simulation error is shown in Fig. 8 along with a Gaussian fit. It is seen that the mean of the static grit density distribution differs by less than 3.5% from the measured values.

A comparison between the errors from the numerical simulation and analytic models is shown in Fig. 9 using the fitted Gaussian distributions from each. It is seen that the models have approximately the same error range but the analytic model has a negative mean error at -1.24 compared to the numerical simulation at 0.25. This negative mean error is attributed to the difference in the methods of calculating the number of grits in the wheel in each model as the numerical simulation is guaranteed to always over-predict the number of grits in the wheel [11].

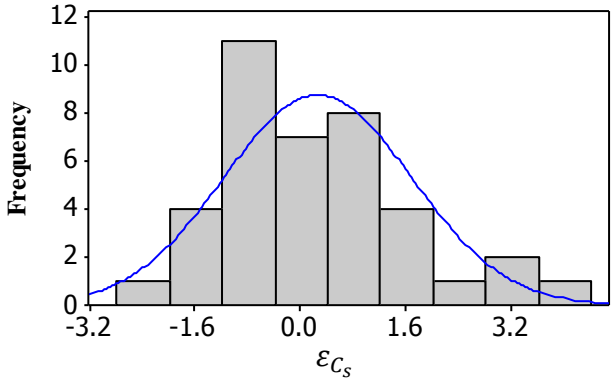

Fig. 8: Histogram of Static Grit Density Relative Error between Numerical Simulation model and Experimental Measurement

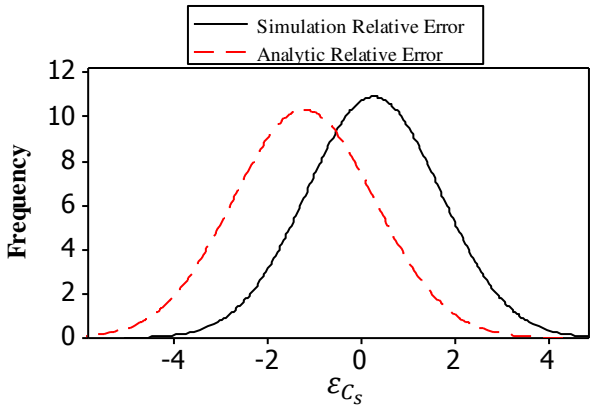

Fig. 9: Fitted Gaussian Distributions of Static Grit Density Relative Error between the Models and Experimental Measurement

The numerical simulation and analytic model provide distributions of the static grit density caused by the stochastic nature of the grit size and locations. The deviation of the measured static grit density values from the means of these distributions could still lie within the range predicted by the standard deviations. An investigation of this was conducted by calculating the standard error of the measured static grit density within the distribution provided by the models as shown in Eq. 4.

$$\mathrm{SE} = \left| \frac{\mu_{C_s} - y_{C_s}}{\sigma_{C_s}} \right| \qquad (4)$$

The standard error can be thought of as how many "standard deviations" the measured value is from the mean. Results showed that the measured static grit densities had standard errors or 3.95 and 3.27 for the simulation and analytic models respectively when the exactly measured wheel specifications where used in the models. This corresponds to a 0.001% and 0.11% likelihood that the measured values came from the model distributions.

However, utilization of the uncertainty in the wheel specification measurements, including the uncertainty in the measured concentration number, decreases the standard errors to 0.21 and 0.39 for the simulation and analytic models respectively. This corresponds to 83.4% and 69.7% likelihoods that the measured values came from the model distributions.

DISCUSSION

The analysis of the microgrinding wheel specifications showed that there is significant error between the target values specified by the manufacturer and the values measured in the final products. The shank diameter errors can be attributed to variations in the turning process used to create the steel shanks of the grinding wheels. This source of overall uncertainty can be easily reduced by tightening the tolerances used to machine the shank. The bond thickness variation arises from the nature of the plating process governed mostly by electroplating time. The wheel width and concentration error come from the method in which the grits are adhered to the shank before the wheel is submerged for electroplating.

The comparison between the model and the measured static grit density showed that when using only the mean static grit density reported by the models, the measured static grit density errors are as high as 4.5%. However, utilizing the expanded stochastic considerations in the models generated by the authors allows for a predicted range of values for the static grit density. The standard error showed that on average each wheel was 0.21 and 0.39 standard deviations from the expected static grit density in the simulation and analytic models respectively. The numerical simulation was seen to provide more accurate results, but the accuracy arises from a cost of computation complexity and speed[11] .

The ability to use the models to predict the static grit density of microgrinding wheels can be explored by utilizing only the manufacturer-provided wheel specifications as *a priori* information. The numerical simulation model showed that the relative error between the mean static grit density predicted by the model and the measured values was 9.7% with a maximum of 24%. This demonstrates that microgrinding wheel topography modeling needs metrology inspection of the wheel geometry to have any confidence in the modeled static grit density. Manufacturer specifications have errors that compound to yield a final product that deviates too significantly. Instead, distributions for the predicted errors in each manufacturer specification can be generated by a set of metrology experiments. This study showed that these distributions can be modeled as Gaussian for the manufacturer chosen.

The best solution for acquiring accurate static wheel topography information is *in situ* wheel measurement. The machine vision technique used in this study is easily adaptable to be performed using an inexpensive camera system in the actual grinding machine tool. The algorithm can quickly and autonomously provide full wheel surface characterization or, by utilizing sampling statistics, measure only a small portion of the wheel and predict the topography characteristics.

CONCLUSSION

The machine vision method was seen to provide a method of quickly measuring the static grit density on the surface of the microgrinding wheels. The comparison between the model and the measured static grit density showed that when accounting for the uncertainty in the measured wheel specifications, the measured static grit density values have 83.4% and 69.7% likelihoods of coming from numerical simulation and analytic model distributions respectively. The ability to use the models to predict the static grit density using only *a priori* manufacturer specifications was seen to be accurate up to only 76%. Future work should target an investigation into the impact of the wheel diameter and grit size on the statistical variance in topography characteristics as well as the ability to predict them.

REFERENCES

[1] N. Otsu, "A threshold selection method from gray-level histograms," *Automatica,* 1975; 11: 23-27.

[2] L. Yin *et al.*, "Influence of microstructure on

ultraprecision grinding of cemented carbides," *International Journal of Machine Tools and Manufacture,* 2004; 44: 533-543.

[3] J. Verkerk, "Final report concerning CIRP cooperative work on the characterization of grinding wheel topography," *Annals of the CIRP,* 1977; 26: 385-395.

[4] J. Brecker *et al.*, "Measurement of the effective number of cutting points in the surface of a grinding wheel," 1974, 740–745.

[5] M. Shaw, "Fundamentals of grinding," 1972, 221-258.

[6] S. Law *et al.*, "On building models for the grinding process," *Journal of Engineering for Industry,* 1973; 95: 983-991.

[7] T. Orioka, "Probabilistic treatment on the grinding geometry," *Bulletin of the Japanese Society of Grinding Engineers,* 1961; 1: 27-29.

[8] H. McAdams, "Markov chain models of grinding profiles," *Journal of Engineering for Industry,* 1964; 86: 383.

[9] P. Basuray *et al.*, "Surface generated in fine grinding. Part 1 Probabilistic model," *The International Journal of Production Research,* 1981; 19: 677-688.

[10] T. Hwang *et al.*, "High speed grinding of silicon nitride with electroplated diamond wheels, part 2: wheel topography and grinding mechanisms," *Journal of manufacturing science and engineering,* 2000; 122: 42-50.

[11] J. Kunz *et al.*, "Stochastic Modeling of Microgrinding Wheel Topography," Journal of Micro and Nano-Manufacturing, JMNM-12-1028, 2012.

[12] J. Kunz *et al.*, "Static Grit Density Measurement Methods for Medium-Grit Diamond Microgrinding Wheels," *International Conference on Micro-Machining*: 2011.

APPENDIX

Table 3: Experimentally Measured Specifications of Microgrinding Wheels

	Manufacturer Specifications				Measured Specifications					
Wheel #	**G#**	**OD**	**L**	**C**	**D_{shank}**	**t_{bond}**	**L**	**C**	**N_a**	**C_s**
		[μm]	**[μm]**		**[μm]**	**[μm]**	**[μm]**			**[#/mm^2]**
1.1					326.0	47.5	1545	160.39	182	89.49
1.2	#200	508	1588	140	291.5	48.7	1789	140.08	172	79.28
1.3					332.2	50.8	1260	141.90	144	85.47
2.1					399.5	41.3	2830	177.22	989	228.51
2.2	#400	508	3175	140	388.1	47.0	3024	149.34	1000	217.47
2.3					396.8	45.2	2986	155.31	1005	219.92
3.1					903.4	43.3	1317	136.28	798	194.78
3.2					907.2	50.1	1419	127.74	943	209.92
3.3					895.4	46.6	1459	115.93	805	177.69
3.4					921.8	40.1	1309	141.30	774	187.75
3.5					906.0	42.2	1406	130.15	794	181.50
3.6					903.4	44.8	1384	122.50	781	180.88
3.7					895.5	44.4	1581	133.42	953	195.04
3.8	#400	1016	1588	140	900.6	42.6	1496	128.42	836	180.47
3.9					918.4	48.3	1406	105.32	749	167.07
3.10					893.4	43.4	1478	110.68	720	158.28
3.11					909.6	42.6	1432	125.59	790	176.57
3.12					912.2	43.9	1459	134.20	891	194.42
3.13					900.8	48.3	1442	106.99	767	169.74
3.14					909.6	42.4	1451	127.22	807	178.05
3.15					910.0	43.0	1454	136.09	878	193.06
4.1					954.6	42.9	1518	139.26	981	195.18
4.2					961.8	45.0	1585	110.71	862	166.94
4.3	#400*	1016	1588	140	952.2	45.4	1454	135.54	969	203.50
4.4					940.2	46.6	1731	105.28	908	154.74
4.5					940.9	48.9	1679	116.34	1025	180.49
4.6					938.6	43.9	1461	109.91	750	160.10
5.1					897.2	40.2	2863	135.63	1587	180.53
5.2	#400	1016	3175	140	909.6	37.3	2881	152.33	1678	188.48
5.3					899.4	38.8	2798	152.11	1678	186.92
6.1					932.8	44.6	2817	119.71	1592	173.43
6.2	#400*	1016	3175	140	947.3	36.7	3042	145.26	1728	174.14
6.3					942.9	33.0	2956	163.00	1680	175.36
7.1					1417.0	41.3	1227	138.18	1107	191.24
7.2	#400	1524"	1588	140	1422.3	42.2	1326	114.50	1016	161.31
7.3					1420.5	40.9	1128	116.71	853	165.22
8.1					1361.7	45.2	2727	136.57	981	79.25
8.2	#200	1524	3175	140	1337.5	52.6	2604	122.81	968	83.16
8.3					1346.9	45.4	2844	140.42	1046	81.84